

Fig. 6. Measured outputs from the array for  $\lambda/\alpha = 0.22$ . (a) The offset corrected even output (solid line) compared with the response of an ideal filter (dashed line). (b) The offset corrected odd output (solid line) compared with the response of an ideal filter (dashed line).

tion kernels similar to those of the Gabor filter simultaneously. Test results indicate that the chips work as expected. Future work on chip design includes fabricating chips with larger numbers of cells and two-dimensional (2-D) filters with tunable orientation and scale. On the application side, we are investigating the use of these chips in binocular vergence control of an active stereo vision system.

#### ACKNOWLEDGMENT

The author would like to thank K. K. Lau and K. Poon for their help in making measurements of the chip reported here.

#### REFERENCES

- [1] J. G. Daugman, "Two-dimensional spectral analysis of cortical receptive field profiles," *Vision Research*, vol. 20, pp. 847–856, 1980.
- [2] L. O. Chua and L. Yang, "Cellular neural networks: Theory," *IEEE Trans. Circuits Syst.*, vol. 35, pp. 1257–1272, Oct. 1988.
- [3] B. E. Shi, "Gabor-type filtering in space and time with cellular neural networks," *IEEE Trans. Circuits Syst. I*, vol. 45, pp. 121–132, Feb. 1998.
- [4] —, "Using a CNN sensor for 1-D image fixation," in *Proc. Int. Symp. Nonlinear Theory Applications (NOLTA '98)*, Crans-Montana, Switzerland, Sept. 1998, vol. 2, pp. 671–674.
- [5] S. Espejo, R. Dominguez-Castro, R. Carmona, and A. Rodriguez-Vazquez, "CMOS optical-sensor array with high output current levels and automatic signal-range centering," *Electron. Lett.*, vol. 30, no. 22, pp. 1847–1849, Oct. 27, 1994.

- [6] K. F. Hui and B. E. Shi, "Robustness of CNN implementations for Gabor-type image filtering," in *Proc. Asia Pacific Conf. Circuits Systems*, Seoul, South Korea, Nov. 1996, pp. 105–108.
- [7] C. C. Enz, F. Kruppenacher, and E. A. Vittoz, "An analytical MOS transistor model valid in all regions of operation and dedicated to low-voltage and low-current applications," *Anal. Integr. Circuits Signal Processing*, vol. 8, no. 1, pp. 83–114, July 1995.
- [8] B. E. Shi and K. F. Hui, "An analog VLSI neural network for phase based machine vision," in *Advances in Neural Information Processing Systems 10*, M. I. Jordan, M. J. Kearns, and S. A. Solla, Eds. Cambridge, MA: MIT, 1998, pp. 726–732.
- [9] C. A. Mead and T. Delbruck, "Scanners for visualizing activity of analog VLSI circuitry," *Anal. Integr. Circuits Signal Processing*, vol. 1, no. 2, pp. 93–106, Oct. 1991.

## Focal-Plane Analog VLSI Cellular Implementation of the Boundary Contour System

Gert Cauwenberghs and James Waskiewicz

**Abstract**—We present an analog very large scale integration (VLSI) cellular architecture implementing a version of the boundary contour system (BCS) for real-time focal-plane image processing. Inspired by neuromorphic models across the retina and several layers of visual cortex, the design integrates in each pixel the functions of phototransduction and simple cells, complex cells, hypercomplex cells, and bipole cells in each of three directions interconnected on a hexagonal grid. Analog current-mode complementary metal-oxide-semiconductor (CMOS) circuits are used throughout to perform edge detection, local inhibition, directionally selective long-range diffusive kernels, and renormalizing global gain control. Experimental results from a fabricated  $12 \times 10$  pixel prototype in a  $1.2\text{-}\mu\text{m}$  CMOS process are included, demonstrating the robustness of the implemented BCS model in selecting image contours in a cluttered and noisy background.

**Index Terms**—Active pixel sensors, analog VLSI, boundary segmentation, cellular neural networks (CNN's), focal-plane image processing, neuromorphic engineering.

#### I. INTRODUCTION

The boundary contour system (BCS) and feature contour system (FCS) combine models for processes of image segmentation, feature filling, and surface reconstruction in biological vision systems [1], [2]. They provide a powerful technique to recognize patterns and restore image quality under excessive fixed-pattern noise, such as in specific absorption rate (SAR) images [3].

The BCS model encompasses visual processing at different levels, including several layers of cells in visual cortex interacting through shunting inhibition, long-range cooperative excitation, and renormalization. The implementation architecture, shown schematically in Fig. 1, partitions the BCS model into three levels: simple cells; complex and hypercomplex cells; and bipole cells. A simpler model, that does not require bipole cells and only involves cells in V1, but

Manuscript received February 28, 1998; revised September 25, 1998. This work was supported by in part by ARPA/ONR MURI under Grant N00014-95-1-0409. This paper was recommended by Guest Editors A. Rodríguez-Vázquez and T. Roska.

The authors are with the Department of Electrical and Computer Engineering, Johns Hopkins University, Baltimore, MD 21218 USA (e-mail: gert@bach.ece.jhu.edu; davros@bach.ece.jhu.edu).

Publisher Item Identifier S 1057-7122(99)02073-5.

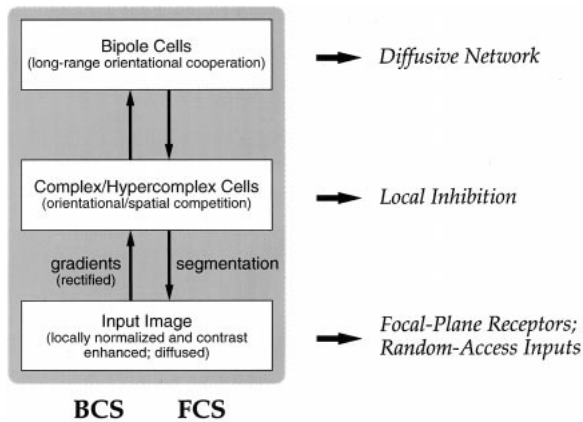


Fig. 1. Diagram of BCS/FCS model for image segmentation, feature filling, and surface reconstruction. Three layers represent simple, complex, and bipole cells.

otherwise preserves much of the structure and properties of BCS as implemented here, is presented in [4].

Simple cells compute unidirectional gradients of normalized intensity obtained from the photoreceptors. Complex (hypercomplex) cells perform spatial and directional competition (inhibition) for edge formation. Bipole cells perform long-range cooperation for boundary contour enhancement and exert positive feedback (excitation) onto the hypercomplex cells. Our present implementation does not include the FCS model, which completes and fills features through diffusive spatial filtering of the image blocked by the edges formed in BCS.

The motivation for implementing a relatively sophisticated model such as BCS on the focal plane is dual. First, as argued in [5], complex neuromorphic active pixel designs become viable engineering solutions as the feature size of the VLSI technology shrinks significantly below the optical diffraction limit and more transistors can be stuffed in each pixel. The pixel design that we present contains 88 transistors, likely the most complex active pixel imager ever put on silicon. Second, our motivation is to extend the functionality of previous work on analog VLSI neuromorphic and cellular image processors for image boundary segmentation, e.g., [5], [6], and [8]–[12], which are based on simplified physical models that do not include directional selectivity and/or long-range signal aggregation for boundary formation in the presence of significant noise and clutter. The analog VLSI implementation of BCS reported here is a first step toward this goal, with the additional objectives of real-time low-power operation, as required for demanding target recognition applications. As an alternative to focal-plane operation, the input image can be loaded electronically through random-access pixel addressing.

From the perspective of cellular neural networks (CNN's) [12], [13] the architecture implementing BCS described here is interesting in two aspects, which extend the capability of conventional cellular structures with nearest neighbor connectivity. First, long-range connectivity across the bipole cells is achieved through the use of (a variant on) diffusor elements [7], [15] which implement a diffusive kernel extending across several cells with just nearest neighbor coupling between cells. Second, directional selectivity in the response to image edge contours is achieved by mapping a vector field onto a cellular structure on a hexagonal grid, with components in three directions for each cell. More specifically, the BCS model integrates three layers of such vector fields, including simple cells, (hyper) complex cells, and bipole cells, with bottom-up and top-down interactions between layers.

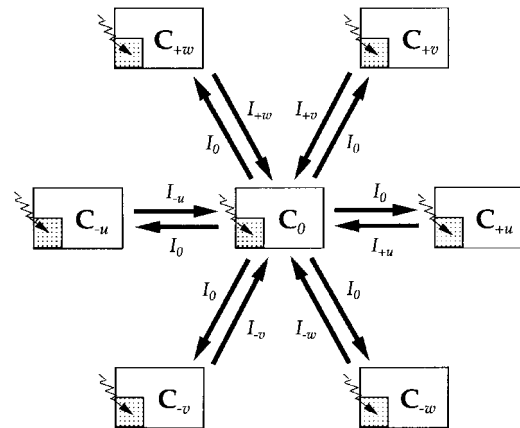


Fig. 2. Hexagonal arrangement of BCS pixels, at the level of simple and complex cells, extending in three directions  $u$ ,  $v$ , and  $w$  in the focal plane.

The full-blown BCS model [1] is sufficiently complex to make a scalable focal-plane VLSI implementation impractical, if not impossible. Algorithmic and architectural simplifications, which preserve much of the original functionality of BCS, are the subject of Section II. An analog VLSI cellular implementation in current-mode CMOS technology is presented in Section III, and experimental results from a small ( $12 \times 10$  pixel) prototype are included in Section IV.

## II. MODIFIED BCS ALGORITHM AND CELLULAR ARCHITECTURE

We adopted the BCS algorithm, as described in detail in [1] and [2], for analog continuous-time implementation on a hexagonal grid, extending in three directions  $u$ ,  $v$ , and  $w$  on the focal plane as indicated schematically in Fig. 2.

In the implemented circuit model, a pixel unit consists of a photosensor (or random-access analog memory) sourcing a current indicating light intensity, gradient computation and rectification circuits implementing simple cells in three directions, and one complex (hypercomplex) cell and one bipole cell for each of the three directions.

### A. Definition and Notation

The BCS equations and architecture involve the notion of vector fields, mapped on a cellular architecture and discretized both in space and angular resolution.

For notational convenience, let subscript zero denote the center pixel and  $\pm u$ ,  $\pm v$ , and  $\pm w$  its six neighbors, depicted in Fig. 2. Components of each complex cell vector  $\mathbf{C}_i$  at grid location  $i$ , along three directions of edge selectivity, are indicated as  $C_i^j$  with superscript index  $j$  for the direction taking values  $u$ ,  $v$ , or  $w$ . Similarly, the bipole vectors are denoted by  $\mathbf{B}_i$  at grid locations  $i$ , or componentwise as  $B_i^j$  in the three directions  $j$ . Nonvector (i.e., scalar) fields, such as input intensity, only take a subscript index for location.

### B. Simple, Complex, and Hypercomplex Cells

The photosensors generate a current  $I_i$  that is proportional to intensity. Through current mirrors, the currents  $I_i$  propagate in the three directions  $u$ ,  $v$ , and  $w$  as noted in Fig. 2. Rectified finite-difference gradient estimates of  $I_i$  are obtained for each of the three hexagonal directions. These gradients excite the complex cells  $C_i^j$ .

Lateral inhibition among spatially ( $i$ ) and directionally ( $j$ ) adjacent complex cells implement the function of hypercomplex cells for edge enhancement and noise reduction. The complex output ( $C_i^j$ ) is inhibited by local complex cell outputs in the two competing directions

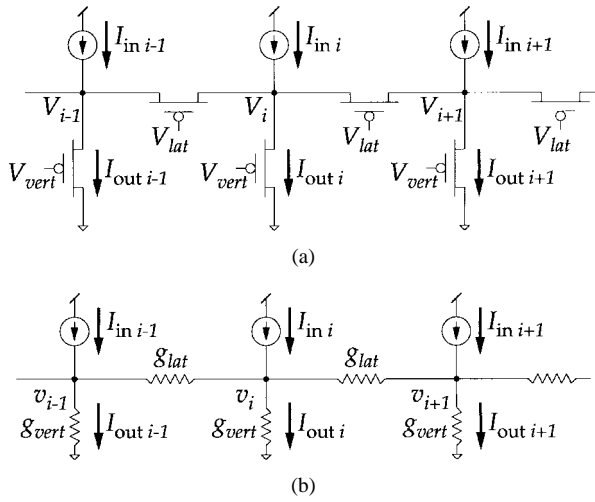


Fig. 3. One-dimensional (1-D) network of diffusive elements. (a) Translinear implementation. (b) Equivalent resistive model  $g_{lat}/g_{vert}$  determines the spatial extent of diffusion.

of  $j$ .  $C_0$  is additionally inhibited by the complex cells of the four nearest neighbors in competing locations  $i$  with parallel orientation.

The complex cells  $C_i^j$  also interact with bipole cells  $B_i^j$  which exert local positive feedback to corresponding components of complex cells for long-range directionally selective smooth contour enhancement and suppression of spurious edges.  $C_i^j$  is excited by bipole interaction received from the bipole cell  $B_i^j$  on the line crossing  $i$  in the same direction  $j$ .

The operation of the simple and (hyper) complex cells in the hexagonal arrangement is summarized in the following equation for one of the three directions  $u$

$$C_0^u = \left| \frac{1}{2}(I_v + I_w) - I_0 \right| - \alpha(C_0^v + C_0^w) - \alpha'(C_v^u + C_w^u + C_{-v}^u + C_{-w}^u) + \beta B_0^u \quad (1)$$

where

$ 1/2(I_v + I_w) - I_0 $	rectified gradient input as approximated on the hexagonal grid;
$\alpha(C_0^v + C_0^w)$	inhibition from locally opposing directions;
$\alpha'(C_v^u + C_w^u + C_{-v}^u + C_{-w}^u)$	inhibition from nonaligned neighbors in the same direction;
$\beta B_0^u$	excitation through long-range cooperation from the bipole cell.

The corresponding equations for the other two directions  $v$  and  $w$  are symmetrical with respect to (1), obtained through rotation of the reference axes by  $\pm\pi/3$

$$C_0^v = \left| \frac{1}{2}(I_w + I_{-u}) - I_0 \right| - \alpha(C_0^w + C_0^u) - \alpha'(C_w^v + C_{-u}^v + C_{-w}^v + C_u^v) + \beta B_0^v \quad (2)$$

and

$$C_0^w = \left| \frac{1}{2}(I_u + I_v) - I_0 \right| - \alpha(C_0^u + C_0^v) - \alpha'(C_u^w + C_v^w + C_{-u}^w + C_{-v}^w) + \beta B_0^w. \quad (3)$$

### C. Bipole Cell-Diffusive Kernels

The bipole cells  $B_i^j$  interconnected on a directionally selective diffusive network provide long-range cooperative feedback to the complex cells  $C_i^j$  and enhance smooth edge contours while reducing spurious edges due to image clutter.

The bipole cell-resistive grid (Fig. 4) implements a three-fold crosscoupled directionally polarized long-range diffusive kernel,

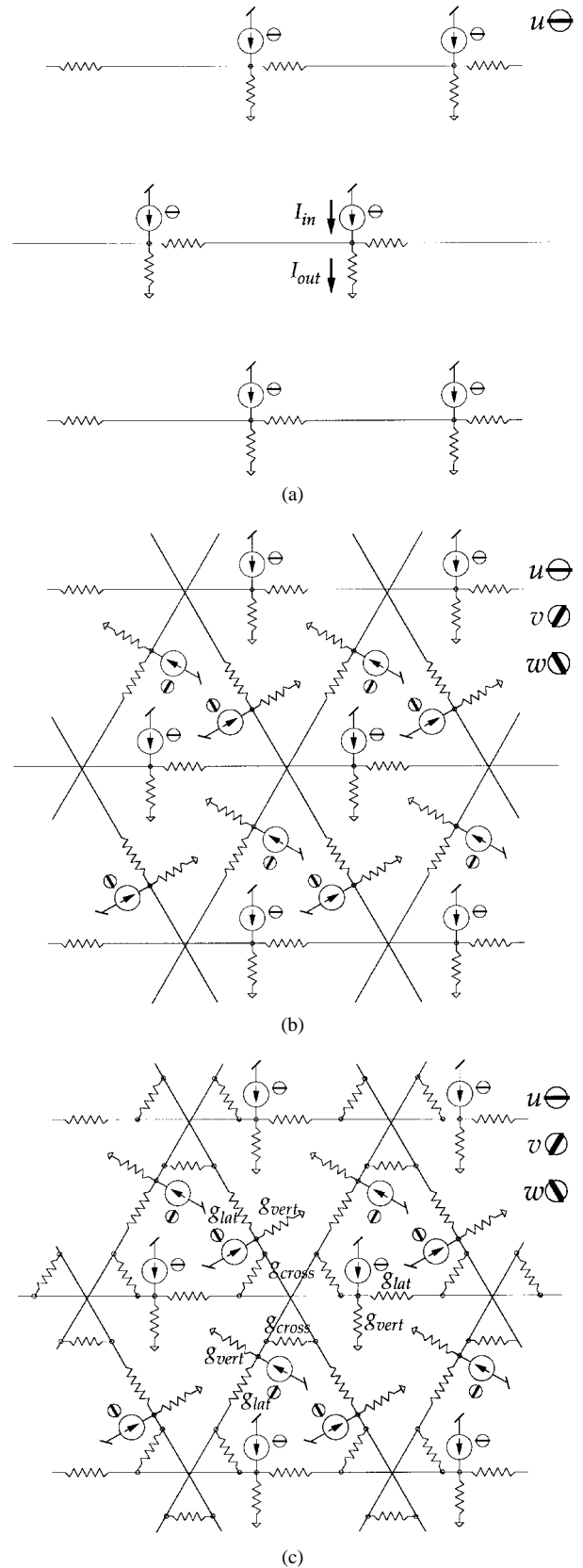


Fig. 4. Network of bipole cells, implemented on a hexagonal resistive grid using orientationally tuned diffusors extending in three directions. (a) Single 1-D diffuser network tuned to horizontal orientation. (b) Interlaced diffuser networks tuned to three orientations. (c) Crosslinking provides spatial dispersion and graded directional response of the bipole.  $g_{lat}/g_{vert}$  determines the spatial extent of the dipole, whereas  $g_{lat}/g_{cross}$  sets the directional selectivity.

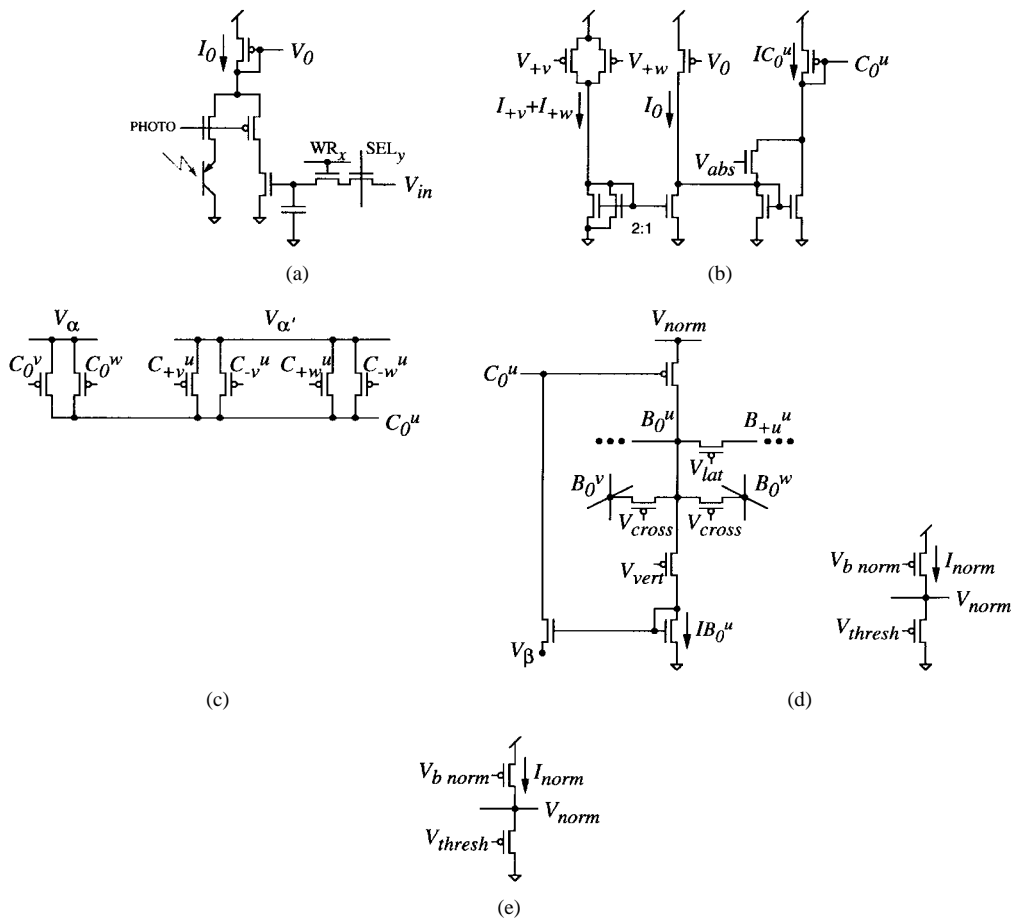


Fig. 5. Simplified circuit schematic of one BCS cell in the hexagonal array, showing only one of three directions; the other directions being symmetrical in implementation. (a) Photosensor and random-access input selection circuit. (b) Simple cell rectified gradient calculation. (c) Complex cell spatial and orientational inhibition. (d) Bipole cell directional long-range cooperation. (e) Bipole global gain and threshold control.

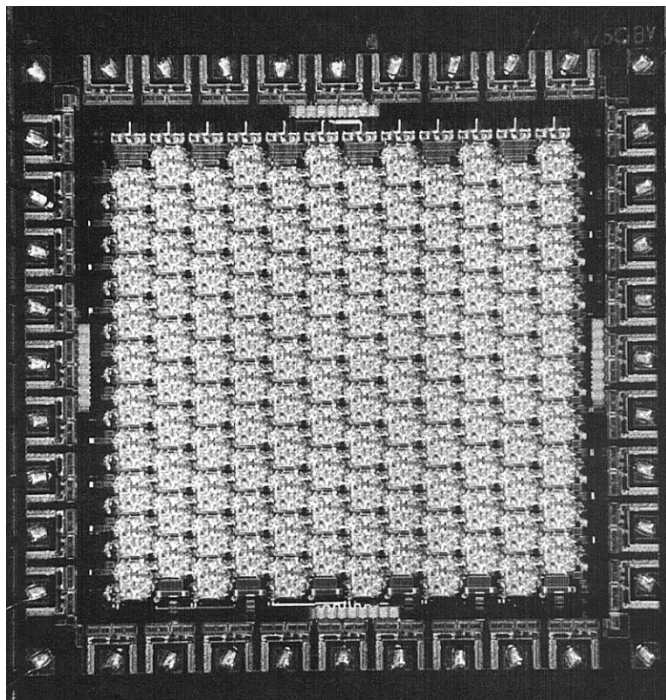


Fig. 6. Chip micrograph of BCS processor. Dimensions are  $2.2 \times 2.2$  sq. mm in  $1.2\text{-}\mu\text{m}$  CMOS technology.

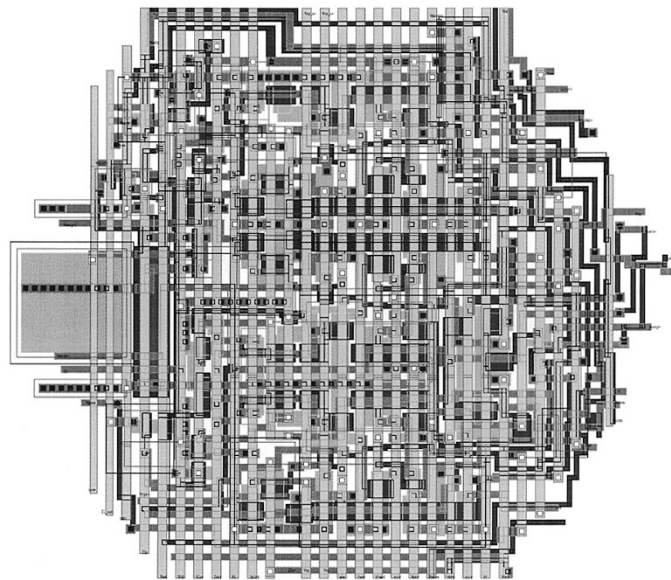


Fig. 7. BCS pixel layout containing 88 transistors.

formally expressed as follows:

$$B_0^u = K_u^u C_0^u + K_v^u C_0^v + K_w^u C_0^w \tag{4}$$

where  $K_u^u$ ,  $K_v^u$ , and  $K_w^u$  represent spatial convolutional kernels implementing bipole fields symmetrically polarized in the  $u$ ,  $v$ , and  $w$  directions.

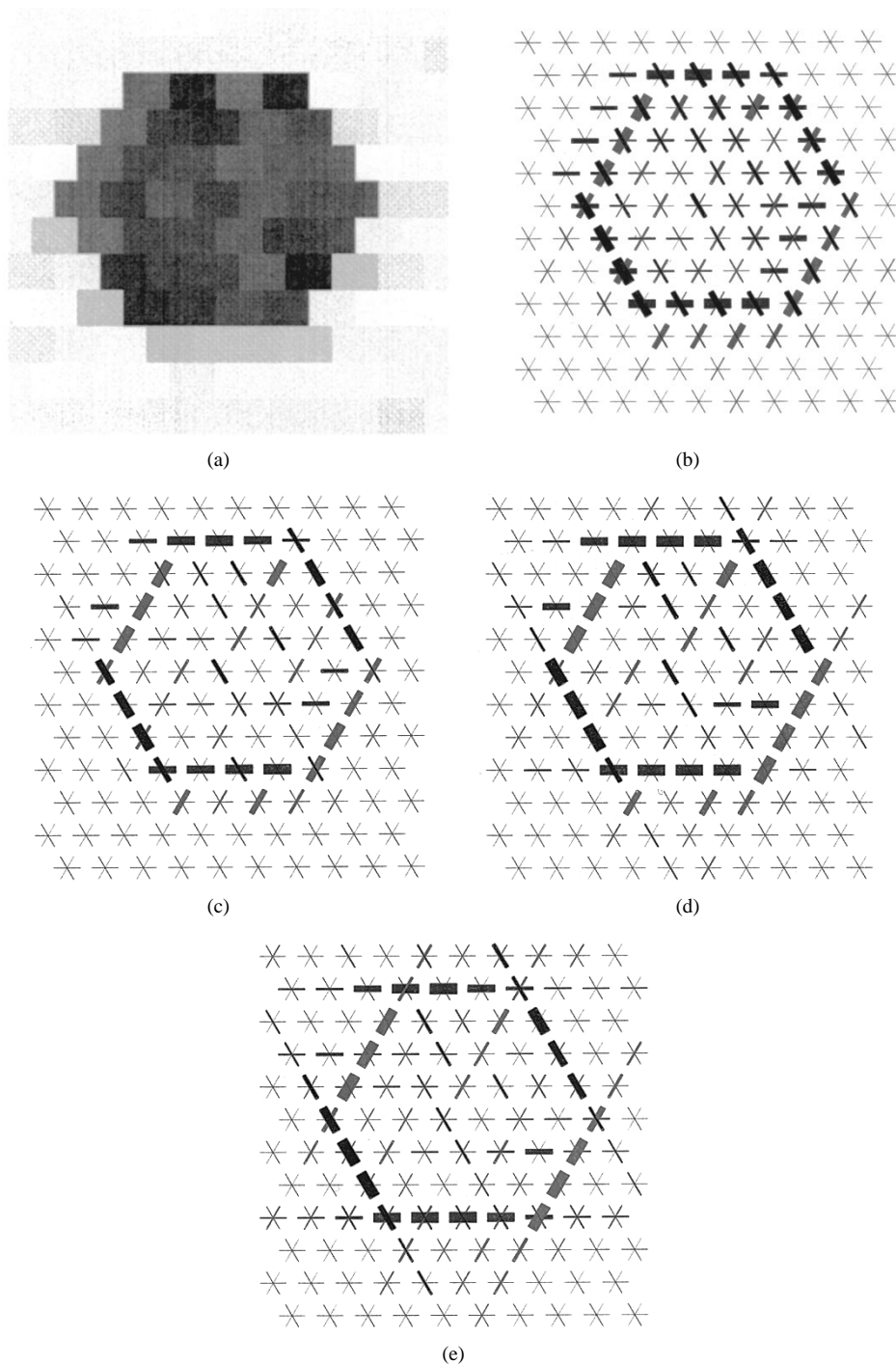


Fig. 8. Experimental response of the BCS chip to an example circular pattern. (a) Reconstructed input image. (b) Gradient (complex) field without hypercomplex inhibition or bipole excitation. (c) Complex field without bipole excitation. (d) Complex field with bipole excitation activated. (e) Bipole field. The thickness of the bars on the grid represent the measured components of the complex and bipole fields in the three directions.

Diffusive kernels can be efficiently implemented with a distributed representation using resistive diffusive elements termed diffusors [7], [15]. One key advantage of diffusor elements is that they preserve a cellular nearest neighbor topology of cell interconnectivity while implementing a long-range diffusive kernel extending across the entire array of cells. Furthermore, a linear kernel is obtained in the current domain, even though the device characteristics of the MOS-transistor circuit elements used are highly nonlinear. The capability to construct linear transfer functions through the use of exponential transconductance devices is one of the advantages offered

by translinear circuits, implemented with MOS transistors operated in the subthreshold region [7].

A 1-D linear diffusive network spanning one of three directions  $u$  is shown in Fig. 3 [7]. This network forms the basis for constructing the  $u$  component of the bipole field by diffusing the  $u$  component of the complex field along the  $u$  dimension. The diffusive network is shown in two forms, with subthreshold PMOS transistors and with linear resistive elements. Under the transformation  $v_i \equiv I_0 \exp(qV_i/kT)$  the two networks become equivalent with  $g_{lat} \equiv \exp(-q\kappa V_{lat}/kT)$  and  $g_{vert} \equiv \exp(-q\kappa V_{vert}/kT)$ . The network response is linear in

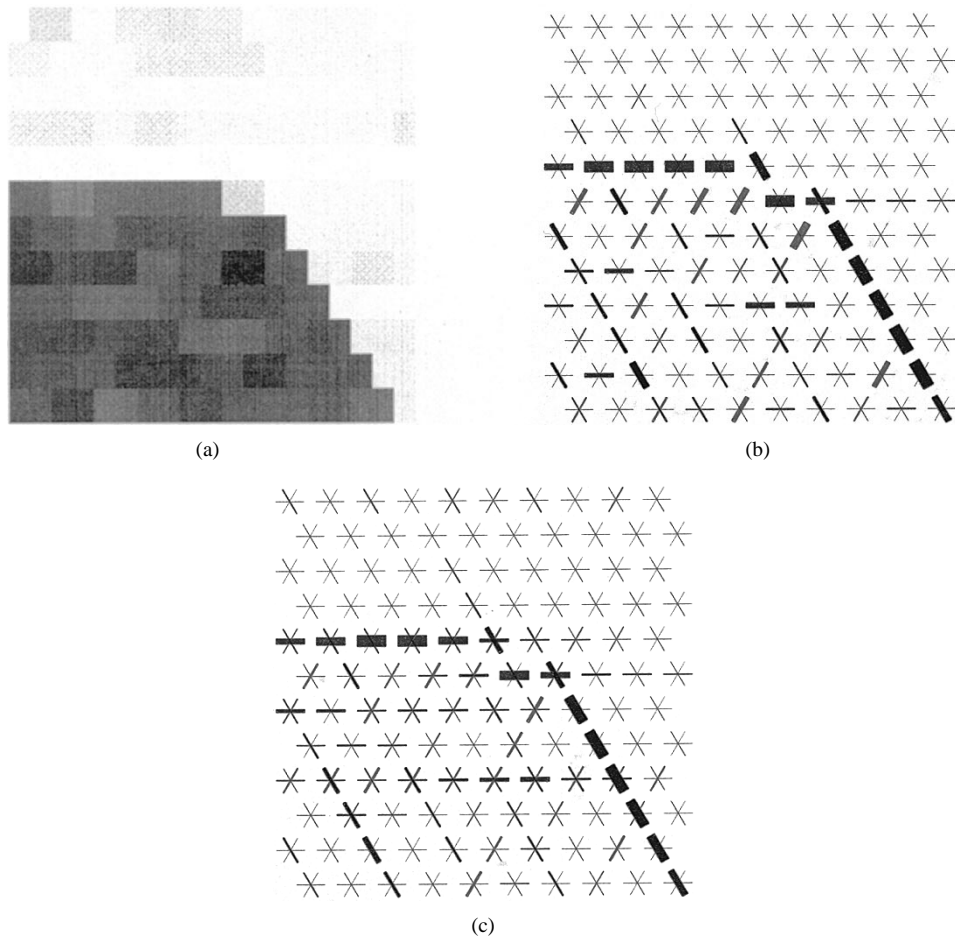


Fig. 9. Experimental response of the BCS chip to a curved edge. (a) Reconstructed input image. (b) Complex field. (c) Bipole field. The thickness of the bars on the grid represent the measured components in the three directions.

the current domain, implementing a diffusive kernel

$$\begin{aligned}
 I_{out\ i} - I_{in\ i} &= \frac{g_{lat}}{g_{vert}} (I_{out\ i+1} - 2I_{out\ i} + I_{out\ i-1}) \\
 &\approx \frac{g_{lat}}{g_{vert}} \Delta u^2 \frac{\partial^2 I_{out}}{\partial u^2}
 \end{aligned} \quad (5)$$

where the ratio  $g_{lat}/g_{vert}$  determines the spatial extent of diffusion along the  $u$  axis in units  $\Delta u$  on the grid.

Three families of linear-diffusor networks are used, each tuned to one of the directions  $u$ ,  $v$ , and  $w$ . To allow for angular spread and a graded response to contours in directions different from the principal axes, the three families are resistively coupled with crosslink conductances  $g_{cross}$ , as shown in Fig. 4. The ratio  $g_{lat}/g_{cross}$  controls the directional selectivity of the diffusion kernel.

The input to the diffusive network are complex cell currents  $C_i^j$  scaled by a factor  $\lambda_{norm}$  that implements global normalization and thresholding. The bipole field response  $B_i^j$  at the output of the network is then modeled as

$$\begin{aligned}
 B_0^u &= \lambda_{norm} C_0^u + \sigma_{lat} (B_{+u}^u - 2B_0^u + B_{-u}^u) \\
 &\quad + \sigma_{cross} (B_0^v + B_0^w - 2B_0^u) \\
 B_0^v &= \lambda_{norm} C_0^v + \sigma_{lat} (B_{+v}^v - 2B_0^v + B_{-v}^v) \\
 &\quad + \sigma_{cross} (B_0^u + B_0^w - 2B_0^v) \\
 B_0^w &= \lambda_{norm} C_0^w + \sigma_{lat} (B_{+w}^w - 2B_0^w + B_{-w}^w) \\
 &\quad + \sigma_{cross} (B_0^u + B_0^v - 2B_0^w)
 \end{aligned} \quad (6)$$

where  $\sigma_{lat} = g_{lat}/g_{vert}$  and  $\sigma_{cross} = g_{cross}/g_{vert}$ .

### III. ANALOG VLSI IMPLEMENTATION

The simplified circuit diagram of the BCS cell, including simple, complex, and bipole cell functions on a hexagonal grid, is shown in Fig. 5.

#### A. Photosensor and Simple Cells

The image is acquired either optically from phototransistors on the focal plane, or in direct electronic format through random-access pixel addressing, Fig. 5(a). The advantage of including a random-access electronic interface is modularity and expandability in the architecture. This allows, for instance, the ability to interface the chip with other stages of processing, such as a silicon retina [8] or shunting-neuron [14] preprocessing stage for contrast enhancement and dynamic range compression of the input image to BCS. Several BCS chips can be combined in parallel to increase the available image size, and a separate imager with elementary preprocessing allows a higher fill factor.

The simple cell portion in Fig. 5(b) combines the local intensity  $I_0$  with intensities  $I_v$  and  $I_w$ , received from neighboring cells, to compute the rectified gradient in (1) using distributed current mirrors and an absolute value circuit [7]. A PMOS load converts the complex cell output into a voltage representation  $C_0^u$  for distribution to neighboring nodes and complementary orientations.

#### B. Complex Cells

A complex cell, performing local inhibition for spatial and directional competition according to (1), is shown in Fig. 5(c) for one of

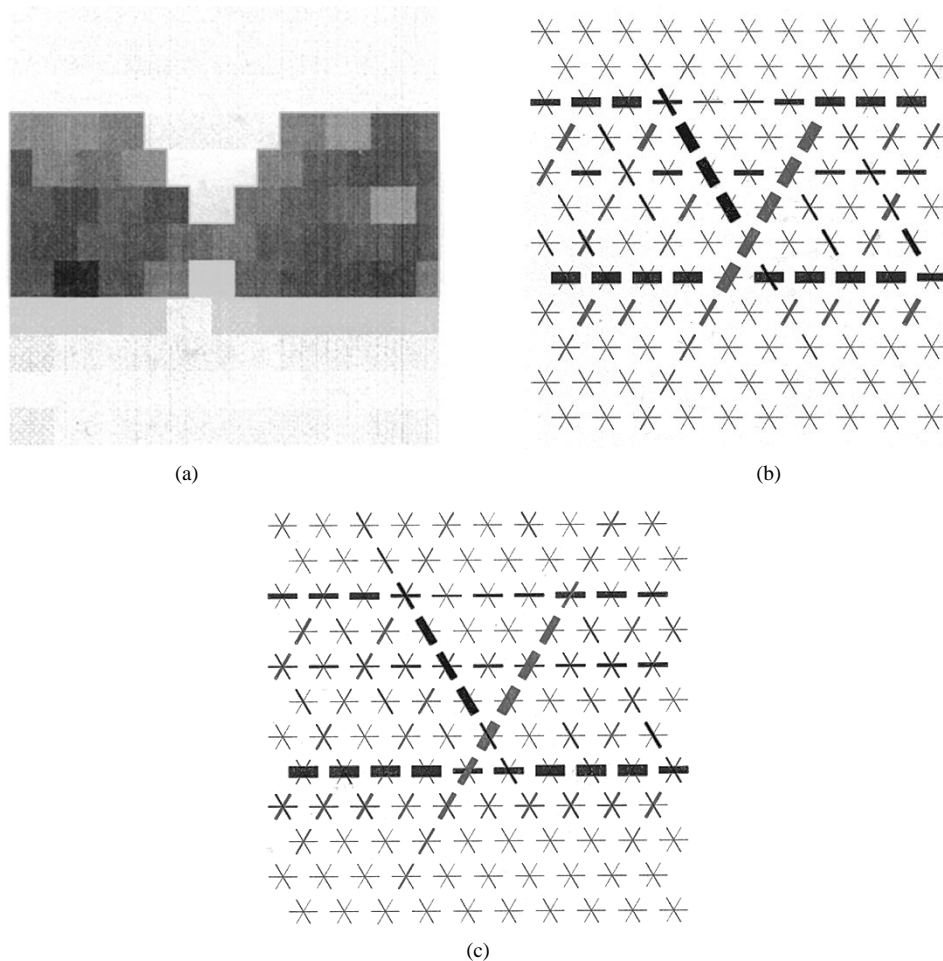


Fig. 10. Experimental response of the BCS chip to a bar with two gaps of different size. (a) Reconstructed input image. (b) Complex field. (c) Bipole field.

the three dimensions. Inhibition is implemented through distributed current mirrors. The strength of the spatial and directional inhibition is controlled independently by applying source voltage biases  $V_\alpha$  and  $V_{\alpha'}$ , which determine the constants  $\alpha$  and  $\alpha'$ , respectively.

### C. Bipole Cells

Long-range cooperation is performed in the bipole layer, of which one cell in direction is shown in Fig. 5(d). The directionally selective diffusive kernel (6) is implemented in current mode using subthreshold MOS transistors by extending the MOS equivalence between Fig. 3(a) and (b) to the structure of Fig. 4, with three families extending in each direction with crosslinks for angular dispersion.

Voltage biases control the spatial extent and directional selectivity of the interactions, as well as the level of renormalization for the interaction between complex and bipole cells. The values for  $g_{vert}$ ,  $g_{lat}$ , and  $g_{cross}$  controlling the bipole kernel are set externally by applying gate bias voltages  $V_{vert}$ ,  $V_{lat}$ , and  $V_{cross}$ , respectively. Likewise, the constant  $\beta$  in (1) is set by the applied source voltage  $V_\beta$ . Global normalization and thresholding of the bipole response for improved stability of edge formation is achieved through an additional diffusive network, which acts as a localized Gilbert-type current normalizer between complex and bipole cells [only partially shown in Fig. 5(e)].

## IV. EXPERIMENTAL RESULTS

A prototype  $12 \times 10$ -pixel array has been fabricated and tested. A micrograph of the tiny  $2.2 \times 2.2$ -sq. mm chip, fabricated through

MOSIS in  $1.2\text{-}\mu\text{m}$  CMOS technology, is shown in Fig. 6. The pixel unit, illustrated in Fig. 7, has been designed for testability and has not been optimized for density. The pixel contains 88 transistors including a phototransistor, a large sample-and-hold capacitor, interface circuitry, and three networks of interconnections in each of the three directions, requiring a fan-in/fan-out of 18-node voltages across the interface of each pixel unit.

We have tested the BCS chip both under focal-plane optical inputs and random-access direct electronic inputs. Input currents from optical input under ambient room lighting conditions are around 30 nA. The experimental results reported here are obtained by feeding test inputs electronically. The three components of complex and bipole outputs of the array, together with the acquired input image, are multiplexed out using a separate address decoder.

The response of the BCS chip to two test images of interest are shown in Figs. 8–10. For graphical clarity, the simple, complex, and bipole fields are reproduced as bars in three directions, of which the thickness indicates the measured activity in each of the three orientations.

The processing through different stages in the BCS chip is illustrated in Fig. 8, showing the reconstructed image, the rectified gradient field, the inhibition by the complex interactions, and the excitation by the bipole interactions feeding back onto the complex cells.

Fig. 9 illustrates the interpolating directional response to a curved edge in the input, varying in direction between two of the principal

axes ( $u$  and  $w$  in the example). Interpolation between quantized directions is important, since implementing more axes on the grid incurs a quadratic cost in complexity.

The third example image contains a bar with two gaps of different diameter for the purpose of testing BCS's capacity to extend contour boundaries across clutter. The response in Fig. 10 demonstrates, to a certain extent, the bipole property in which short-range discontinuities are bridged, but large ones are preserved.

## V. CONCLUSIONS

An analog VLSI cellular architecture implementing the BCS on the focal plane has been presented. A diffusive kernel with distributed resistive networks has been used to implement long-range interactions of bipole cells without the need of excessive global interconnects across the array of pixels. The cellular model is fairly easy to implement and succeeds in selecting boundary contours in images with significant clutter.

One area for improvement of the cellular architecture is the angular resolution, which is quantized to multiples of  $60^\circ$  ( $\pi/3$ ) in a hexagonal arrangement. Interpolation effectively improves resolution, as shown in Fig. 9, but at some expense in directional selectivity of the bipole cells. In principle, it is possible to extend the resolution, without compromising directional selectivity, by incorporating additional cells tuned at different orientations in each pixel, although the number of interconnects rises sharply (quadratically) with the number of cells per pixel. One possible idea to extend the present approach to a continuous angular resolution is the use of tunable directional filters, e.g., as described in [10]. Nevertheless, the quantization effects in orientation appear to be minor in typical imagery, when viewed at a larger scale, for spatial frequencies beyond the Nyquist limit.

Experimental results from a  $12 \times 10$  pixel prototype demonstrate expected BCS operation on simple examples. While this size is small for practical applications, the analog cellular architecture is fully scalable toward higher resolutions. Based on the current design, a 10 000-pixel array in  $0.5\text{-}\mu\text{m}$  CMOS technology would fit a  $1\text{-cm}^2$  die.

## REFERENCES

- [1] S. Grossberg, "Neural networks for visual perception in variable illumination," *Optics News*, pp. 5–10, Aug. 1988.
- [2] ———, "A solution of the figure-ground problem for biological vision," *Neural Networks*, vol. 6, pp. 463–482, 1993.
- [3] S. Grossberg, E. Mingolla, and J. Williamson, "Synthetic aperture radar processing by a multiple scale neural system for boundary and surface representation," *Neural Networks*, vol. 9, no. 1, Jan. 1996.
- [4] Z. P. Li, "A neural model of contour integration in the primary visual cortex," *Neural Computation*, vol. 10, no. 4, pp. 903–940, 1998.
- [5] K. A. Boahen, "A retinomorphic vision system," *IEEE Micro Mag.*, vol. 16, pp. 30–39, Oct. 1996.
- [6] J. G. Harris, C. Koch, and J. Luo, "A two-dimensional analog VLSI circuit for detecting discontinuities in early vision," *Science*, vol. 248, pp. 1209–1211, June 1990.
- [7] A. G. Andreou, K. A. Boahen, P. O. Pouliquen, A. Pavasovic, R. E. Jenkins, and K. Strohhahn, "Current-mode subthreshold MOS circuits for analog VLSI neural systems," *IEEE Trans. Neural Networks*, vol. 2, pp. 205–213, 1991.
- [8] A. G. Andreou, R. C. Meitzler, K. Strohhahn, and K. A. Boahen, "Analog VLSI neuromorphic image acquisition and pre-processing systems," *Neural Networks*, vol. 8, nos. 7/8, pp. 1323–1347, 1995.
- [9] L. Dron McIlrath, "A CCD/CMOS focal-plane array edge detection processor implementing the multiscale veto algorithm," *IEEE J. Solid-State Circuits*, vol. 31, pp. 1239–1248, 1996.
- [10] Y. Miyake, W. T. Freeman, J. Ohta, K. Tanaka, and K. Kyuma, "A gesture controlled human interface using an artificial retina chip," in *Proc. IEEE Lasers Electro-Optics Conf. (LEOS '96)*, July 1996.
- [11] P. Venier, A. Mortara, X. Arreguit, and E. A. Vittoz, "An integrated cortical layer for orientation enhancement," *IEEE J. Solid-State Circuits*, vol. 32, pp. 177–186, Feb. 1997.
- [12] R. Dominguez-Castro, S. Espejo, A. Rodriguez-Vazquez, R. A. Carmona, P. Foldesy, A. Zarandy, P. Szolgay, T. Sziranyi, and T. Roska, "A  $0.8\text{-}\mu\text{m}$  CMOS 2-dimensional programmable mixed-signal focal-plane array processor with on-chip binary imaging and instructions storage," *IEEE J. Solid-State Circuits*, vol. 32, pp. 1013–1026, July 1997.
- [13] T. Roska and L. O. Chua, "The CNN universal machine—An analogic array computer," *IEEE Trans. Circuits Syst. I*, vol. 40, pp. 163–173, 1993.
- [14] T. Hinck and A. E. Hubbard, "Image edge enhancement, dynamic compression and noise suppression using analog circuit processing," in *Proc. 17th Conf. Advanced Research VLSI*, Ann Arbor, MI, 1997, pp. 114–126.
- [15] E. Fragniere, A. van Schaik, and E. Vittoz, "Reactive components for pseudo-resistive networks," *Electron. Lett.*, vol. 33, no. 23, pp. 1913–1914, Nov. 1997.